Interband and Intraband Optical Studies of CdSe Colloidal Nanocrystal Films

by

Fumiaki Toyama

B.A. Physics
University of California, Berkeley, 2001

Submitted to the Department of Physics
in partial fulfillment of the requirements for the degree of

Master of Science in Physics

at the

MASSACHUSETTS INSTITUTE OF TECHNOLOGY

September 2004

© Massachusetts Institute of Technology 2004. All rights reserved.

Author .....
Department of Physics
September 1, 2004

Certified by .....
Marc A. Kastner
Donner Professor of Physics and Department Head
Thesis Supervisor

Accepted by .....
Thomas J. Greytak
Professor of Physics and Associate Department Head for Education

MASSACHUSETTS INSTITUTE OF TECHNOLOGY
SEP 14 2004
LIBRARIES

ARCHIVES

Interband and Intraband Optical Studies of CdSe Colloidal Nanocrystal Films

by

Fumiaki Toyama

Submitted to the Department of Physics
on September 1, 2004, in partial fulfillment of the
requirements for the degree of
Master of Science in Physics

Abstract

We present results for optical measurements on charged CdSe nanocrystals. The injection of electrons into quantum confined states is confirmed by monitoring changes in the visible and infrared absorption spectra. Interestingly, the response is observed only in the nanocrystals that have been chemically treated with sodium biphenyl. Bleaching of the visible interband transition is observed upon electron injection into the nanocrystal films. It is expect that, with injected electrons in the $1S_e$ state, more electrons are available to undergo the intraband transition and absorb more light in infrared region. However, the opposite effect is observed. The energy and cross section of the infrared absorption are consistent with a one-electron transition between the $1S_e$ and $1P_e$ states confined in the quantum dots.

Thesis Supervisor: Marc A. Kastner
Title: Donner Professor of Physics and Department Head

Acknowledgments

I consider it a privilege to be given the opportunity to attend a great institution such as MIT and being able to work with the most talented and brightest people. For this I wish to thank the Department of physics.

I would like to thank several people who made this research possible. First, my advisor Professor Marc Kastner guided me through this work with a lot of insight. He has a terrific ability to focus on the interesting physics of a system, and to describe it within a simple intuitive picture. When I approached Marc with the idea of doing a master thesis, he was extremely supportive and helped make a difficult decision for me easier and more rewarding. I am truly grateful for the opportunity to have completed this project.

This research is an extension of Nicole Morgan and Marija Drndic's work. I had the good fortune to work on a project in a new area, at the rapidly expanding intersection of two fields. These experiments would never have been possible without outstanding collaborators in Moungi Bawendi's group in the Chemistry Department. I would like to thank Venda Porter and Mirna Jarosz for always willing to provide terrific samples. I would also like to thank all my fellow group members especially Maria Schriver and Laurie Calvet. We worked together constructing the optical setup and taking data for much of my time here. The FTIR experiment at CMSE could not be performed without the help of Tim McClure.

Contents

List of Figures

Chapter 1

Introduction

1.1 Quantum Dots

Semiconductor quantum dots are tiny clusters of semiconductor material, fabricated on length scales between nanometers to a few microns. The size and shape of these structures can be precisely controlled. Quantum dots are of increasing interest for use in next-generation optical applications, such as photo detectors [1] and emitters [2], in quantum computing applications [3, 4], in nanoelectronics [5, 6], and even in biological applications [7].

The physics of quantum dots shows many parallels with the behavior of naturally occurring quantum systems in atomic and nuclear physics. As in an atom, the energy levels in a quantum dot become quantized due to the confinement of electrons. Quantum dots are often described as "artificial atoms" because of the atomic-like characteristics [9, 10].

Unlike atoms, however, quantum dots can be connected to electrodes and are therefore excellent tools to study atomic-like properties. There is a wealth of interesting phenomena that has been measured in quantum dot structures over the past decade. For instance, a quantum dot placed between metal electrodes has been demonstrated to work as a single electron transistor which turns on and off with the addition of only one electron to the device [11].

1.2 Colloidal Nanocrystals

The techniques of colloidal chemistry make it possible to create vast numbers of nearly identical semiconductor nanocrystals. To date, these solution-based syntheses have been developed to grow nanocrystals of most II-VI and some III-V semiconductors as well as many metals , including gold, silver, and cobalt [12, 13].

One of the most important characteristics of chemically synthesized quantum dots and films made of them is the ability to adjust the process to vary physical parameters, such as size and spacing. A number of different samples, which might cover a broad range of physical parameters, can therefore be made in a straightforward and relatively quick way. Although it is difficult to construct large arrays of lithographically patterned artificial atoms, colloidal nanocrystals assemble themselves into such arrays quite naturally

In our experiments, we use CdSe colloidal nanocrystals because they are the most well-studied nanocrystals due to their band gaps in the visible region. The synthesis of the CdSe nanocrystals, done by our collaborators in the chemistry department, allows the production of high-quality nearly monodisperse samples with less than 5% rms variations in diameter [12]. The methods for the synthesis and sample preparation are described in some detail in the next chapter.

1.3 Interband and Intraband Transitions

Control of the wavefuctions in semiconductor nanocrystals is observed not only by interband transitions but also by intraband (intersubband) transitions. "Interband transitions" mean the transitions between the conduction (electron) and valence (hole) bands. In contrast, "Intraband transitions" are the transitions between the quantized levels within the conduction or valence band.

Intraband optical transitions have recently received increased attention for the following reasons. First, they usually occur in the infrared spectral range. Second, they

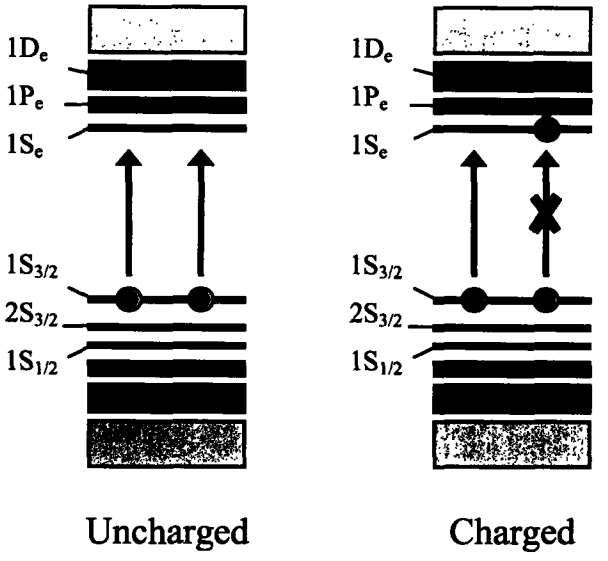

Figure 1-1: Schematic of the electronic energy levels in the CdSe nanocrystals. If an electron is successfully transferred into the lowest unoccupied state ($1S_e$), an electronically allowed infrared transition to the next higher state ($1P_e$) must appear. Because the $1S_e$ state is occupied, there is also bleaching of the lowest interband exciton transition.

involve only one type of carrier which, allows us to study separately the dynamics of electrons and holes. Last, they strongly depend on the charge state of the quantum dot, which can be changed deliberately.

Electron transfer in and out of nanocrystals in arrays has been a subject of study for many years. However, it is difficult to know whether injected electrons actually enter the nanocrystals or are localized in trap states. To make sure that the electrons are successfully placed in the lowest unoccupied state of the nanocrystals, rather than charging them by occupation of surface states, infrared spectroscopy of the $1S_e$–$1P_e$ intraband transition has been used. As seen in Figure 1-1, if an electron is successfully transferred into the lowest unoccupied state ($1S_e$), an electronically allowed infrared transition to the next higher state ($1P_e$) must appear. Because the $1S_e$ state is occupied, there is also bleaching of the lowest interband exciton transition.

Previously, $1S_e$–$1P_e$ intraband transitions were reported in optically excited undoped CdSe nanocrystals [14] as well as n-type CdSe nanocrystals which were obtained by chemically treating the nanocrystals with sodium biphenyl [15]. In this thesis, we report efforts to observe the same transitions by electrically injecting electrons into the conduction band using a gate electrode.

1.4 Overview of Experiments

The electronic transport experiments on the CdSe nanocrystal arrays have shown that even when there is charge in the film, the film is highly insulating [16]. The evidence is that after charging with a gate, the conductance of the film at zero bias is too small to detect, that the charge remains in the sample indefinitely after the gate voltage is removed and that the transient current in response to a source-drain voltage step is even smaller when electrons are added by the gate than in the neutral state. We know that the charge is in the film and not in the gate oxide, for example, because exposure to visible light causes almost complete discharge of the sample. However, we cannot say for sure that the electrons added reside in the dots, as opposed to traps in the organic cap layer or surface states on the dots. If the electrons are really injected into the nanocrystals, they will stay in the conduction band and therefore we should be able to observe the emergence of intraband absorption and bleaching of the interband transition.

Using standard silicon processing technology, a large number of identical substrates, with well-controlled electric properties, can be made for measurements of the chemically synthesized nanocrystals. We have completed the fabrication of the substrates before depositing the nanocrystals, because the films are not sufficiently robust to permit the use of standard wafer processing techniques after deposition. The nanocrystal film covers the entire substrate including the electrodes (Figure 1-2).

The measurements consist of applying voltage steps at the gate and measuring the resultant change in the intensity of the reflected beam. It is expected that electrons are injected into the film with positive gate voltage (Figure 1-3). Therefore, the absorption change can be obtained as

$$\text{Absorption change} = \frac{\Delta I}{I_0} = \frac{I_{\text{charged}} - I_0}{I_0}$$

where:charged

I_0 is the intensity of the reflected beam when the film is uncharged (discharged)

I_{charged} is the intensity of the reflected beam when the film is negatively charged

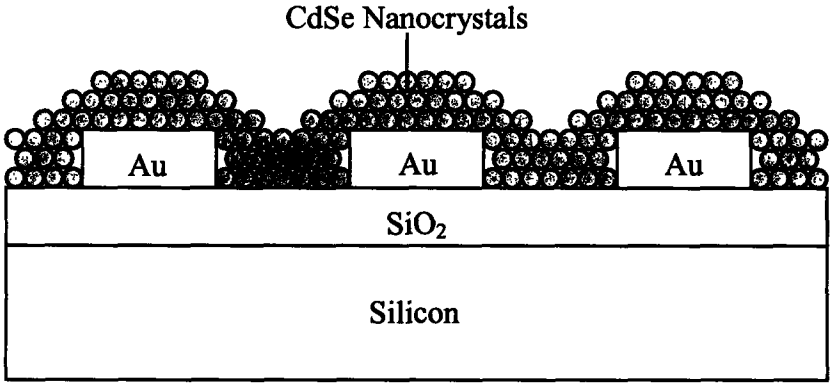

Figure 1-2: Schematic of the device with CdSe nanocryatals deposited on the top. The nanocrystal film covers the entire substrate including the electrodes.

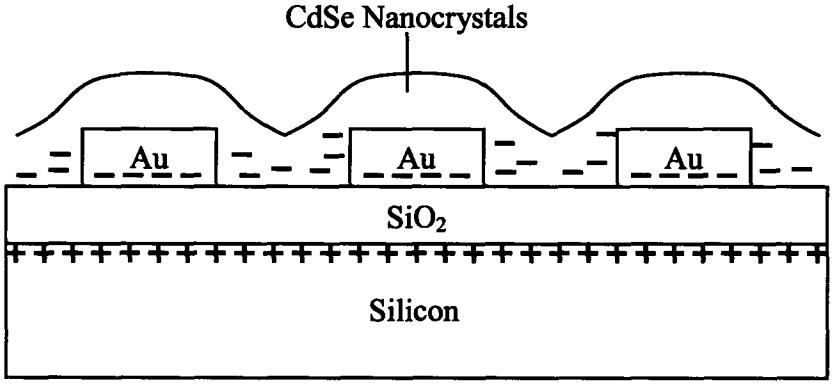

Figure 1-3: Schematic of the device with electrons injected into the nanocrystals. Electrons are injected into the film with positive gate voltage.

The detailed calculation of the absorption change is listed in Appendix. An analysis of both interband and intraband transitions has been conducted. For the interband transitions which take place in visible regime, we have used a diffraction grating monochromater to detect the absorption change. The same monochromater with a different grating has been used to observe the intraband transitions, which occur in the infrared region. We also use a Fourier Transform Infrared (FTIR) spectrometer to obtain the absorption spectra. The electric current flowing into the film, whose integral gives the total amount of the injected charge, has also been measured simultaneously. The experiments are done both before and after doping the film with sodium biphenyl, which is believed to enhance the conductivity of the nanocrystals by adding extra electrons in the conduction band.

Chapter 2

Experimental Details

2.1 Substrate Fabrication

The fabrication of the substrates starts with commercially available 4-inch silicon wafers, degenerately doped with As and with a room temperature resistivity of ρ = .001-.005 Ω-cm. High quality oxides of 350 nm thickness are grown on these wafers. All processing is done in the Microsystems Technology Laboratories at MIT, and standard recipes are used for all the processes.

After oxidation, the fronts of the wafers are coated with photoresist to protect the surface while making electrical contact to the back of the wafers. This contact is made by stripping the oxide from the back of the wafers with a dip in hydrofluoric acid. After the back contact is completed, the photoresist is stripped off the front of the wafers with a plasma ash.

After removing all the photoresist from the wafers, they are treated with HMDS (hexamethyldisilazane) and the fronts of the wafers are again coated with photoresit. The electrode pattern is defined by one step of photolithography, in which a glass mask with an opaque chrome pattern is brought into hard contact with the coated wafer. Where the mask is clear, the resist is exposed, and so the mask pattern is transferred to the wafer.

The standard procedure for lift-off in the MTL uses image reversal photoresist. In the patterning stage, the unexposed area is that where the electrodes will ultimately be.

This initial exposure is followed by half an hour of baking in an oven and the second exposure in which the entire wafer is illuminated. The advantage of image reversal over a simpler procedure is that a slight overhang is created when the resist is removed from the desired areas in developing. This overhang is required to create discontinuities of metal at the edge of the resist, which is critically important in obtaining good results in lift-off.

After the wafers are developed, the metal for the electrodes is deposited with electron-beam evaporation; 100 Å of titanium is used as an adhesion layer followed by 1000 Å of gold. Gold is chosen as the primary electrode material because it is nonreactive metal. After the electrodes are deposited, the remaining resist is stripped with acetone, which also removes the metal deposited on the top of the resist. Only the metal deposited in cleared regions of the wafer remains.

In our experiments, each single substrate is patterned with two inter-digitated working electrodes made of 600 pairs of inter-digitated gold strips (6-mm length, 6-μm width, 110-nm thickness, separated by 5 μm, covering an area of 0.36 cm^2). Although the inter-digitated geometry is adopted for the patterning, we connected the two electrodes together and grounded them in the experiments because the electric potential is applied simply between the electrodes and the back gate. In future experiments, the inter-digitated geometry could be used to measure the relation between electrical conduction and optical change.

2.2 Materials preparation

The synthesis of the CdSe nanocrystals and the deposition of the close-packed films for the work in this thesis were done by our collaborators in the chemistry department [17]. For the sake of completeness, however, a brief description of the methods they used is provided here.

A cadmium precursor solution consisting of cadmium hydroxide (98%), tri-*n*-octylphosphine octylphosphine (TOP, 90%), and xis-9-octadecenoic acid (99%) is degassed under vacuum for one hour. After cooling to room temperature, a selenium

precursor, tri-*n*-octylphosphine selenide (TOPSe, from 1.5 M stock solution), is added and the two precursors are injected into a 335 °C coordinating solvent solution containing TOP, oleylamine, and dioctyl ether. Upon cooling, butanol is added to the growth solution.

The solution is then placed in the refrigerator for one hour and centrifuged to remove excess insoluble organics and any salts that may have formed during the reaction. A precipitation using butanol and hexane as the solvents and methanol as the nonsolvent is repeated three times to narrow the size distribution and to remove excess organics which would prohibit formation of an optically clear and close-packed film. The hexane/butanol/quantum-dot solution is filtered prior to the second and third precipitation using 0.2 μm and 0.1 μm syringe filters, respectively, to further remove excess insoluble organics and salts.

For our experiments, the nanocrystals typically have a core diameter of approximately 4.3 nm with a band gap energy of 2.2 eV. The films are deposited by drop casting the solution of nanocrystals in 9:1 hexane/octane, followed by drying in an inert atmosphere. The thickness of the films is controlled by the concentration of the solution; for this work, it is approximately 100 nm (20 layers)

To dope the film, the device is returned to the glove box where it is immersed in a 0.1 M solution of sodium biphenyl. The solvent for the solution is anhydrous acetonirile. The sample is soaked for 10 minutes, rinsed with 1 mL of solvent, and dried in an oven at 70 °C for one hour to remove excess solvent.

2.3 Device Setup

All optical and electrical measurements are made in a Janis cryostat. The film is deposited on a substrate in a glove box filled with nitrogen gas and the device is placed in the cryostat after the film becomes dry. For the set of experiments described here, it is important that the sample be in vacuum to prevent oxidation of the nanocrystals. The Janis cryostat provides good temperature control from 77 K to 700 K. 77 K is achieved

by pouring liquid nitrogen into the reservoir whose capacity is large enough to hold the temperature for several hours.

The samples are mounted onto ceramic 24 pin dual in-line (DIP) chip carriers with silver epoxy. The electric contact to the gate is therefore made by the layer of silver epoxy between the gold plate of the chip carrier and the back of the silicon wafer. To further ensure thermal stability, the sample rod sits inside a copper canister connected to the heat exchanger. A K-type (Chromeg-Alomega) thermocouple probe and a heater are attached to the sample rod. They are connected to a LakeShore 331 temperature controller to allow real-time temperature control.

The optical windows of the cryostat are replaced by CaF_2 windows which are transparent for the wavelengths from 150 nm (8.3 eV) to 8 μm (0.15 eV). This gives transparency over the entire energy range used in our experiments.

2.4 Diffraction Grating Monochromator

2.4.1 Background and Theory

The diffraction grating is of considerable importance in spectroscopy due to its ability to separate polychromatic light into its constituent monochromatic components. Figure 2-1 shows how a reflective grating works. Light rays *A* and *B*, of wavelength λ, incident on adjacent grooves at angle *I* to the grating normal are shown. Consider light at angle *D* to the grating normal; this light originates from the *A* and *B* rays as they strike the grating. Summing of the rays *A'* and *B'* results in constructive interference if the path difference is equal to any integer multiple of the wavelength λ:

$$a(\sin I - \sin D) = m\lambda$$

where *m* is the order of diffraction.

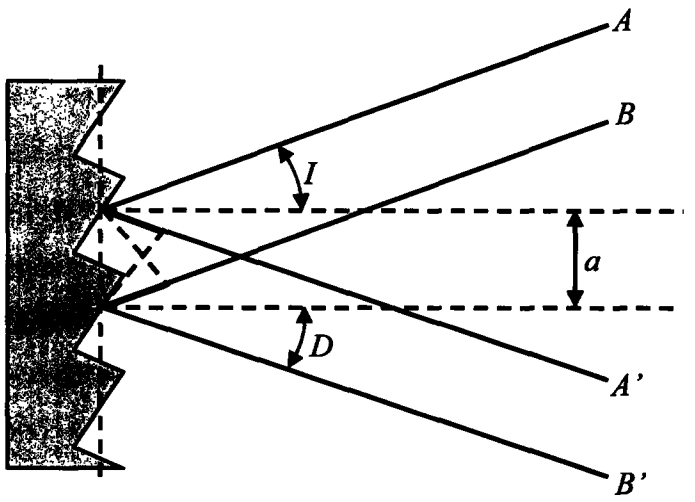

Figure 2-1: Geometry of diffraction by a plane grating. Constructive interference occurs if the path difference is equal to any integer multiple of the wavelength λ.

Although we have considered only two grooves, including all the other grooves does not change the basic equation but sharpens the peak in the plot of diffracted intensity against angle D.

In most monochromators, the input slit and collimating mirror fix the direction of the input beam which strikes the grating. The focusing mirror and exit slit fix the output direction. Only wavelengths which satisfy the grating equation pass through the exit slit. The remainder of the light is scattered and absorbed inside the monochromator. As the grating is rotated, the angles I and D change, although the difference between them remains constant and is fixed by the geometry of the monochromator.

A more convenient form of the grating equation for use with monochromators is:

$$m\lambda = 2a\cos\phi\sin\theta$$

where:

ϕ = Half the included angle between the incident ray and the diffracted ray.

θ = Grating angle relative to the zero order position.

These terms are related to the incident angle I and diffracted angle D by:

$$I = \phi + \theta \text{ and } D = \phi - \theta$$

The grating equation shows that the wavelength diffracted by a grating in a monochromator mount is directly proportional to the sine of the angle θ through which the grating rotates. That is the basis for monochromator drives in which a sine bar rotates the grating to scan wavelengths

2.4.2 Experimental Setup

Although many detailed variations are possible, most monochromators are of the same basic design, which is generally known as the Czerny-Turner configuration. Ours is called "crossed" Czerny-Turner configuration: a variation of Czerny-Turner configuration with the two mirrors angled in such a way that the diverging beam from the input slit and the focused beam heading to the detector intersect each other.

Light from the light source is focused onto an input slit, and light passing through this slit is collimated by a concave mirror, which also reflects it onto a diffraction grating. The grating in turn directs the light onto a second concave mirror, which reflects and focuses it onto an exit slit before it leaves the instrument. Since the redirection of the light beam by the grating is actually diffraction rather than an ordinary reflection, the grating disperses the beam, i.e. different wavelengths leave the grating at different angles. By rotating the grating about its central axis, we can vary the range of wavelengths which can be reflected and focused by the second mirror onto the exit slit.

The optical setup of the experiment is shown in Figure 2-2. The motor controlled Czerny-Turner type monochromator selects a wavelength of light from the source (75 W quartz tungsten halogen lamp). This illumination beam is imaged onto the sample after modulated by the chopper. The reflected beam is collected by the detector and its signal is processed via the lock-in amplifier that is referenced to the chopper

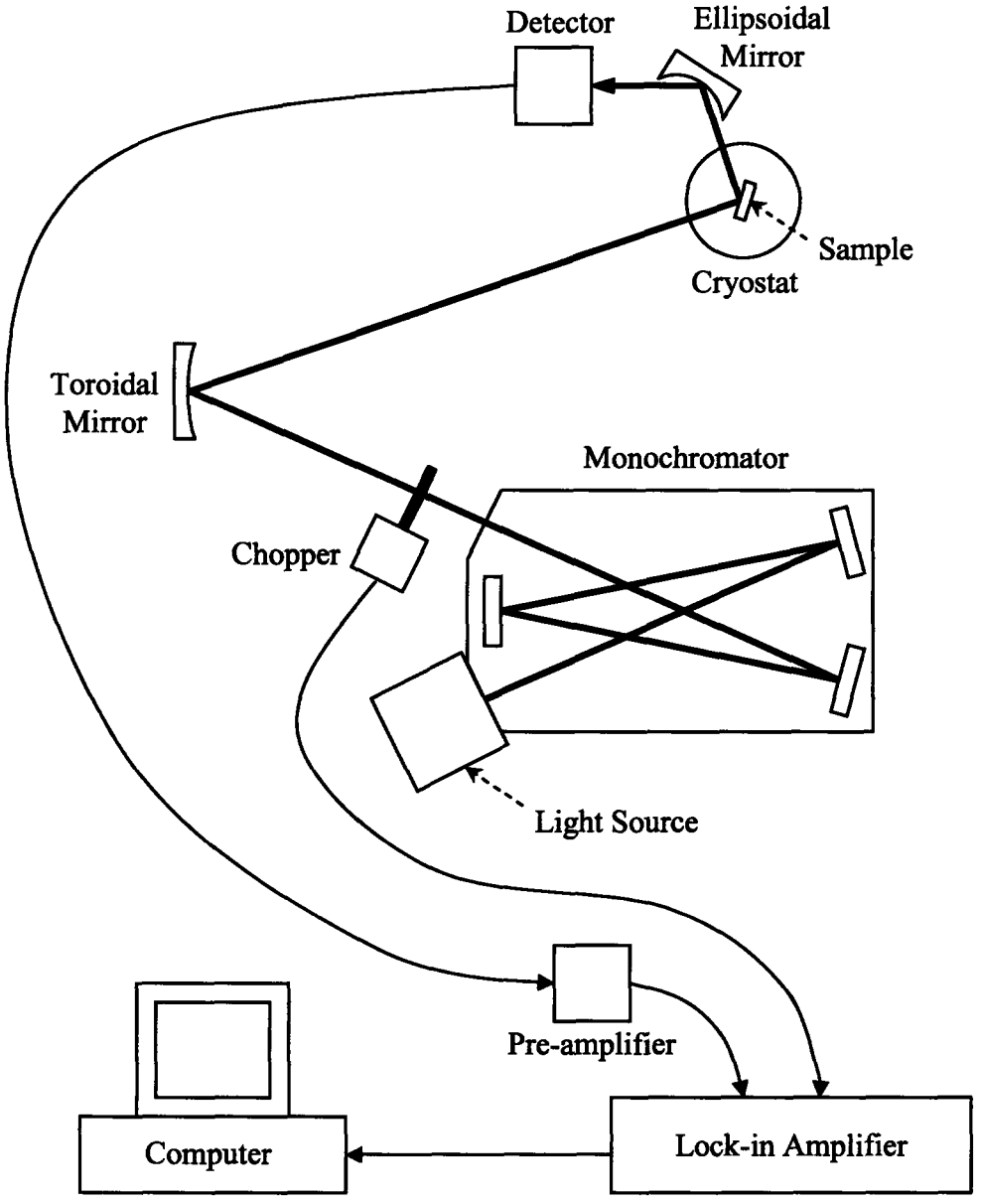

Figure 2-2: Optical setup used in the diffraction grating monochromator experiment. The motor controlled monochromator selects a wavelength of light from the source. This illumination beam is imaged onto the sample after modulated by the chopper. The reflected beam is collected by the detector and its signal is processed via the lock-in amplifier that is referenced to the chopper frequency.

frequency. To detect the signal we use a silicon detector for visible regime and an InSb detector for infrared regime.

The electric potential is produced by a Yokogawa 7651 voltage source in combination with a BOP 500M operational amplifier. This combination has a range of -640 V to $+640$ V. An additional series resistance of 1 MΩ is used to prevent large current flow through the circuit when the gate oxide of the sample is shorted or leaky. It does not affect the measurement when the sample is normal.

The amount of the injected charge is also measured simultaneously. A Keithly 427 current amplifier, an analog model with a ±12 V analog output, is connected to the electrodes and the amplified signal is read with a standard digital multimeter (DMM). In order to reduce current noise, it is crucial to keep both the laboratory power ground and especially the GPIB ground separate from the measurement ground. Some instruments are better than others at isolating GPIB signals from the power ground; although this can be explored through trial and error, it is generally good practice to keep the power cables of any instrument which communicates with the computer (via GPIB) separate from those of the more sensitive measurement devices, particularly the current amplifier.

The electric control, acquisition, and data manipulation are performed by a LabVIEW based program. After acquisition, the reflected signal and the current are stored and plotted as a function of time.

2.5 Fourier Transform Infrared Spectroscopy

2.5.1 Background and Theory

An FTIR spectrometer is an instrument which acquires broadband near infrared to far infrared spectra. The advantage of using a FTIR spectrometer is that it can collect all wavelengths simultaneously, unlike a dispersive instrument, such as a grating monochromator. Figure 2-3 shows the instrumental process of the FIIR experiment

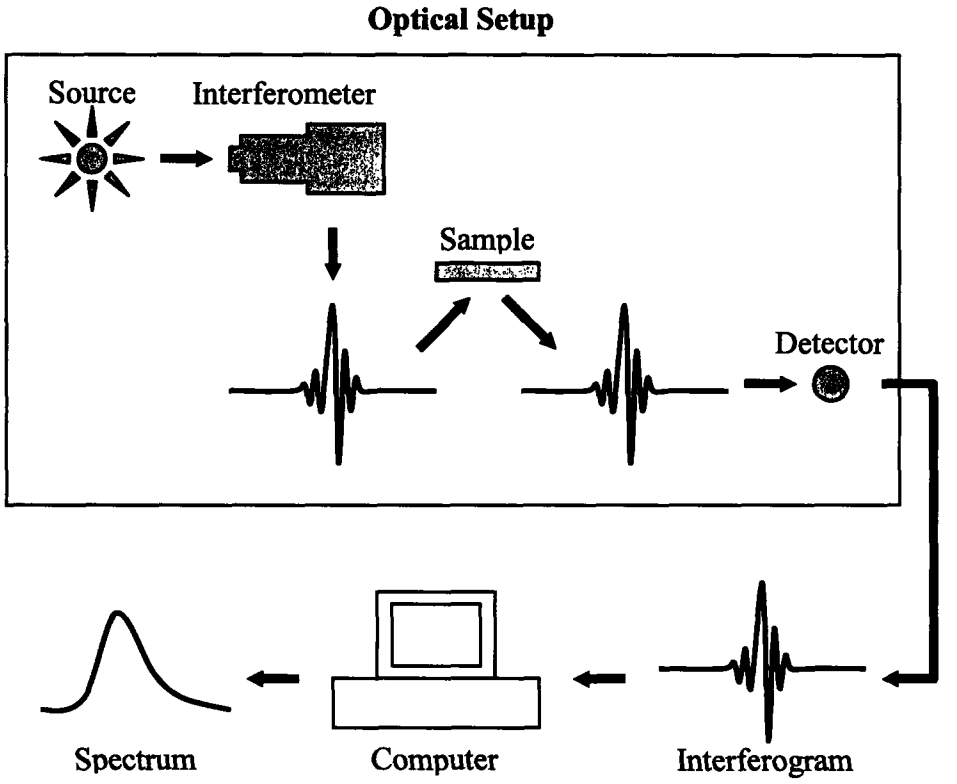

Figure 2-3: Instrumental process of the FIIR experiment. The Michelson Interferometer produces an interference pattern, called interferogram. The interferogram signal is then reflected off of the sample surface. The specific frequencies of energy are adsorbed by the sample and the infrared signal after interaction with the sample is uniquely characteristic of the sample. Once the reflected signal is collected by the detector, its interferogram is translated into the spectrum through the Fast Fourier Transform algorithm.

The FTIR is based on a Michelson interferometer; an example is shown in Figure 2-4. The interferometer consists of a beam splitter, a fixed mirror, and a mirror that translates back and forth. The beam splitter is made of a special material that transmits half of the radiation striking it and reflects the other half. Radiation from the source strikes the beam splitter and separates into two beams. One beam is transmitted through the beam splitter to the fixed mirror and the second is reflected off the beam splitter to the moving mirror. The fixed and moving mirrors reflect the radiation back to the beam splitter. Again, half of this reflected radiation is transmitted and half is reflected at the beam splitter, resulting in one beam passing to the detector and the second back to the source.

The FTIR has a natural reference point when the moving and fixed mirrors are the same distance from the beam splitter. This condition is called zero path difference (ZPD). The moving mirror displacement, Δ, is measured from the zero path difference. The beam reflected from the moving mirror travels 2Δ further than the beam reflected from the fixed mirror. The relationship between the optical path difference (OPD) and mirror displacement is:

$$\mathrm{OPD} = 2\Delta\,\mathrm{n}$$

where n is the refractive index of air and $n \approx 1$.

As the OPD grows, each wavelength produces a maximum intensity at the detector at a different position and, for a broadband signal, they never reach their peaks at the same time except at ZPD. Thus, as the mirror moves away from the large maximum in intensity at ZPD, the interferogram becomes a complex looking oscillatory signal with decreasing amplitude. The x-axis of the interferogram represents the OPD. Each individual wavelength contributes to this signal a single sinusoid with a frequency inversely proportional to its wavelength.

Once an interferogram is collected, it needs to be translated into a spectrum. The process of conversion is through the Fast Fourier Transform algorithm. The discovery of this method by J. W. Cooley and J. W. Turkey in 1965 [18], followed by an explosive growth of computational power, has been the driving force behind the development of the FTIR instruments.

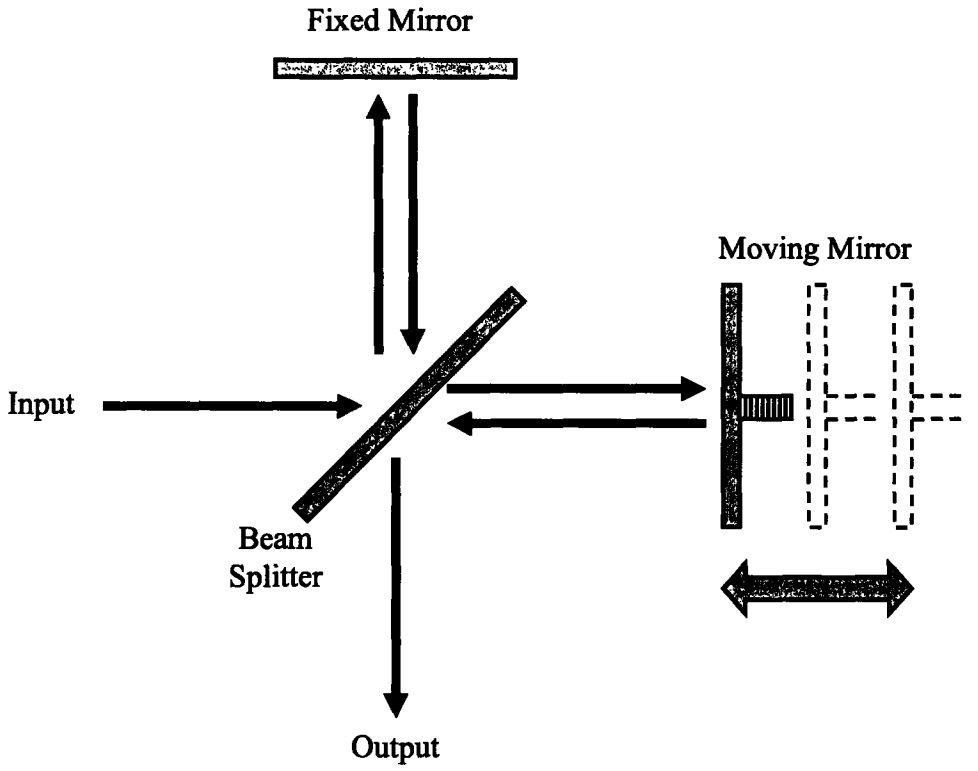

Figure 2-4: Schematic diagram of a Michelson interferometer in a FTIR spectrometer. Radiation from the source strikes the beam splitter and separates into two beams. One beam is transmitted through the beam splitter to the fixed mirror and the second is reflected off the beam splitter to the moving mirror. The fixed and moving mirrors reflect the radiation back to the beam splitter. Again, half of this reflected radiation is transmitted and half is reflected at the beam splitter, resulting in one beam passing to the detector and the second back to the source.

2.5.2 Experimental Setup

The optical setup of the FTIR experiment is sketched in Figure 2-5. We use a Nicolet Magna 860 FTIR spectrometer in the Center for Materials Science and Engineering at MIT. Since the sample is inside the cryostat, the FTIR spectrometer is set to the external mode and the cryostat is placed outside the extrernal window of the spectrometer so that the outgoing infrared beam hits the sample inside the cryostat. The angle between the IR beam and the sample is approximately 45 degrees and the reflected beam is collected by the detector.

There are various combinations of light source, beam splitter and detector available for the FTIR spectrometer. A typical spectrum of each combination is shown in Figure 2-6. For our experiment, two different combinations are used; the infrared light source, CaF_2 splitter and Mercury Cadmium Telluride (MCT) detector is used for the mid-IR regime, and the visible light source, CaF_2 splitter and InSb detector for the near-IR regime. Notice that the data is more reliable where intensity of the detected light signal is stronger.

The electrical connections to the sample are identical to those for the monochromator experiment (Section 2.4.2), and we conducted the measurements alternating positive and negative voltages from 25 to 150 Volts. The electrical potential is applied to the gate of the device and we measure the reflected signal from the sample for 30 seconds after each step, from –V to +V and +V to –V. The voltage steps are repeated for ten cycles and the data at each voltage is averaged. After averaging the detected spectra at both positive and negative voltage, the ratio of the spectra is calculated, resulting in the spectrum of the absorption change due to the injection of electrons into the films.

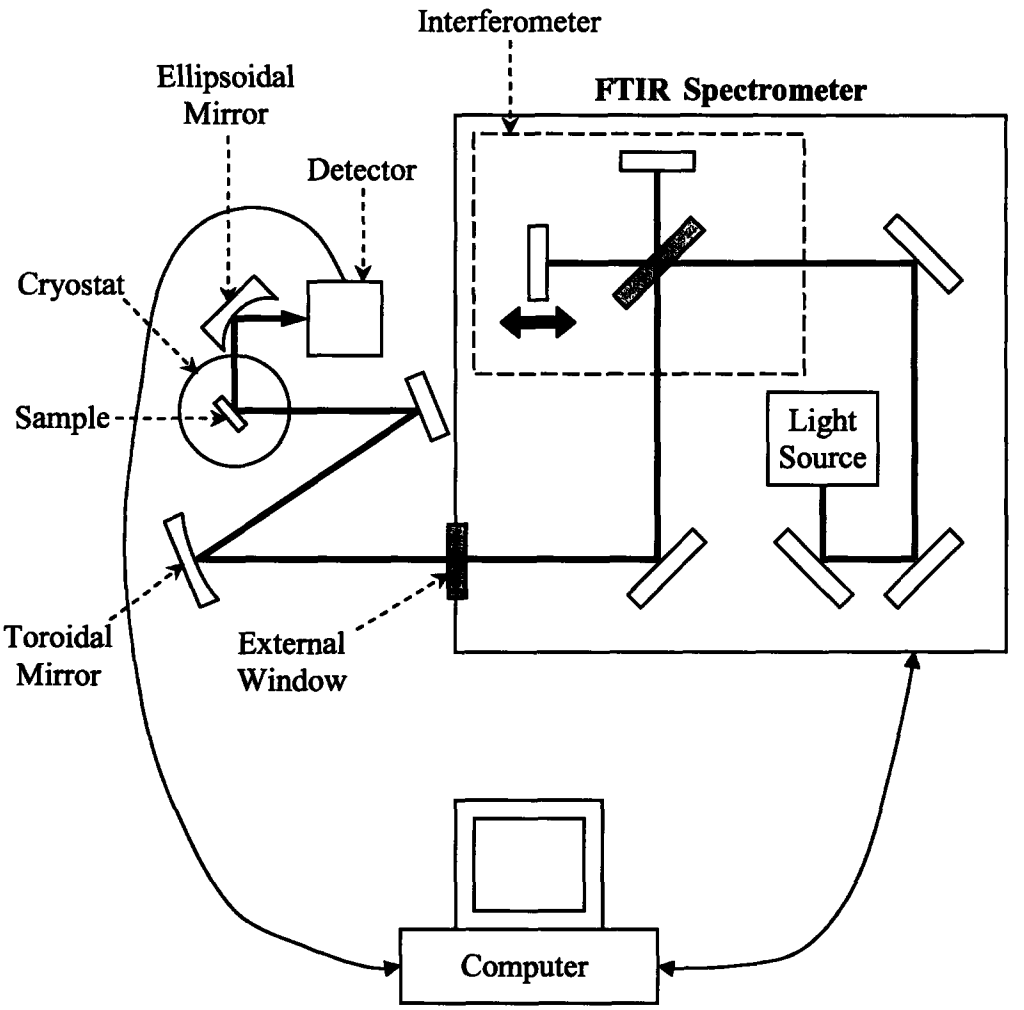

Figure 2-5: Optical setup used in the FTIR experiment The FTIR spectrometer is set to the external mode and the cryostat is placed outside the extrernal window of the spectrometer so that the outgoing infrared beam hits the sample inside the cryostat.

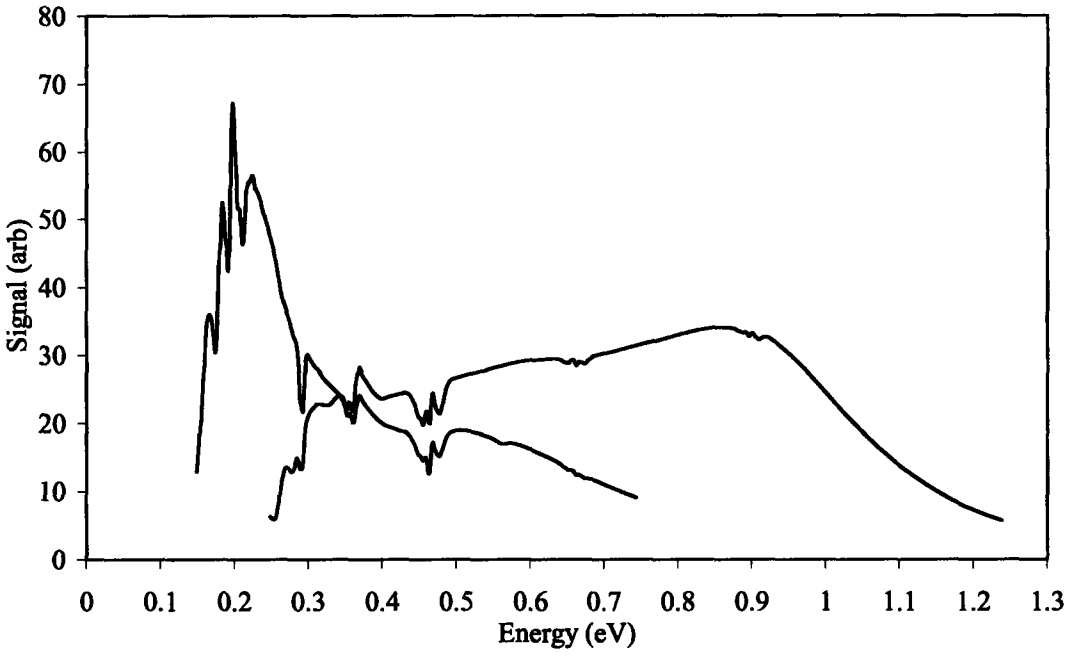

Figure 2-6: Typical detected spectra of the FTIR experiment. For our experiment, two different combinations are used; the infrared light source, CaF_2 splitter and Mercury Cadmium Telluride (MCT) detector is used for the mid-IR regime (blue curve in the graph), and the visible light source, CaF_2 splitter and InSb detector for the near-IR regime (pink curve in the graph).

Chapter 3

Results

3.1 Before Doping

We start the measurements without chemically doping the sample. In principle, we should be able to see interband and intraband transitions without doping, but no steady change of absorption associated with interband or intraband transition is observed before treating the sample with sodium biphenyl.

In the visible regime where the interband transition is expected to be seen, we observe transient spikes in the reflected signal every time the applied voltage changes (Figure 3-1). Because the sign of the absorption change is the same for positive and negative voltages and because it is transient, it appears to be correlated with the current in the device rather than the charge. Figure 3-2 shows the sizes of transient absorption spikes at different energies. Comparing to the shape of the spectrum with the experimental and theoretical results of Stark spectroscopy of CdSe nanocrystals [19], we conclude that the effect results from the Stark effect due to the applied electric field. We do not see a steady change of absorption with Stark effect because the net electric field returns to zero once the sample is fully charged. Since the current is also proportional to the net electric field, the curve of the spikes due to the Stark effect is very similar to the curve of the decaying current except that the spikes are always pointing one direction regardless of the sign of the current.

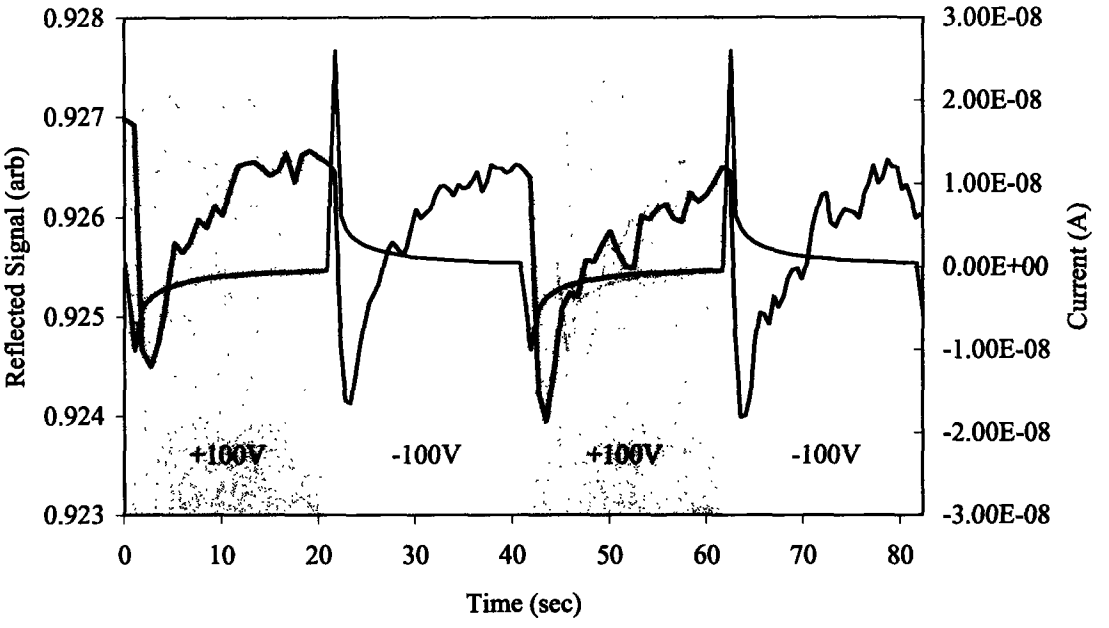

Figure 3-1: Transient absorption spikes (blue curve in the graph) with applied voltage of ±100 V at 2.3 eV with step voltage changes observed before treating with sodium biphenyl. Pink curve shows the current flowing into the film

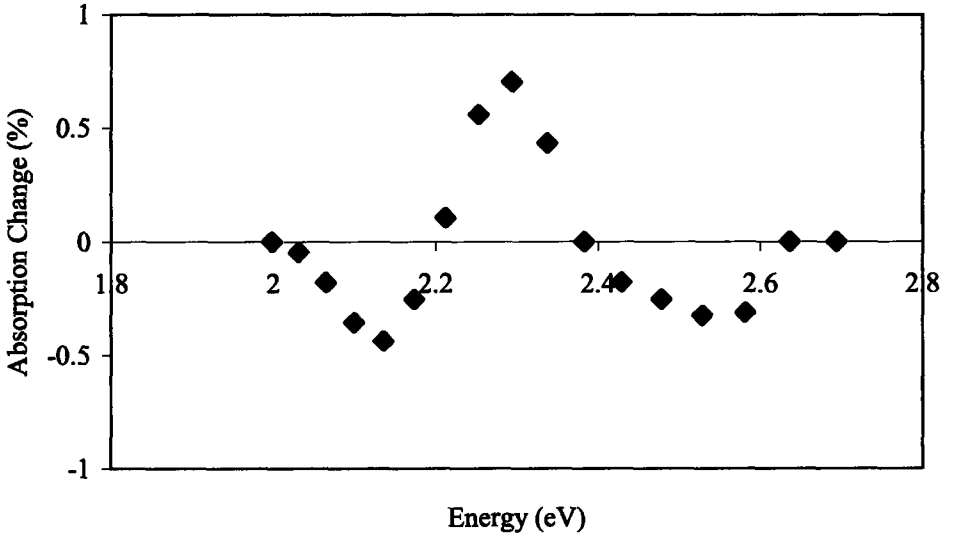

Figure 3-2: Sizes of transient absorption spikes at different energies with applied voltage of ±100 V.

We tried to observe complementary optical changes in infrared regime, but did not find either spikes or steps above the noise level.

3.2 After Doping

Interestingly, a steady response is observed only after the sample is chemically doped. This is accomplished by soaking the nanocrystals film in sodium biphenyl. The biphenyl ion carries a negative charge, which it can donate to nanocrystals.

After the sample is doped, we start to see step changes in absorption, which are the signs of interband and intraband transitions. The effects become smaller after a few days with the sample in vacuum. The sample can be retreated to recover the effects.

I also have to mention that the step changes are not always observed even after doping. The lack of reproducibility may come from the variation of the samples.

3.2.1 Visible Transitions

In Figure 3-3, the relationship between the reflected optical signal and alternating different applied gate voltages at photon energy of 2.2 eV is shown. Immediately after applying a positive voltage, there is a fast increase of the reflected signal, i.e. a decrease of absorption. It is expected that electrons are injected into the film with positive gate voltage. At the same time, bleaching of the interband transition must occur as a result of the occupation of the $1S_e$ state. Thus, the observed behavior agrees with the prediction. It is also noted that absorption changes occur in relatively short time (< 1 second).

Figure 3-4 shows the absorption change at different wavelengths. The numbers indicate the percentage change of the signal when the sign of the applied voltage is alternated. We observe steps for energies between 1.9 eV and 2.4 eV. The effect is strongest at approximately 2.1 eV which is close to the fluorescence peak of the nanocryatals at 2.2 eV.

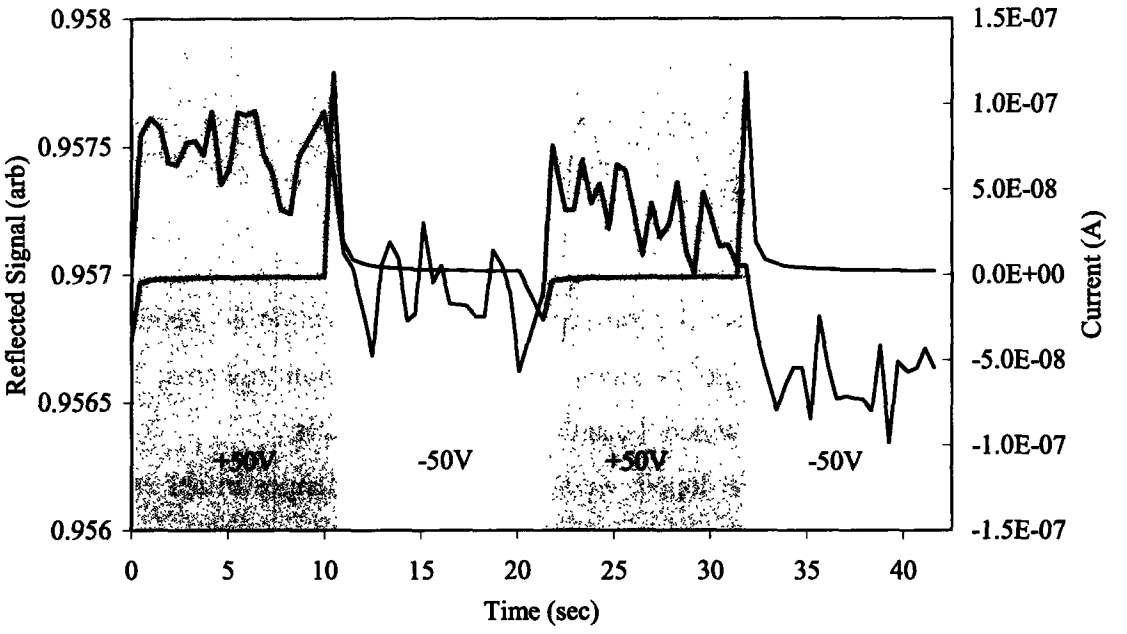

Figure 3-3: Absorption changes (blue curve in the graph) at 2.2 eV with applied voltage of ±50 V. As expected, Bleaching of the interband transition occurs as a result of the occupation of the $1S_e$ state when electrons are injected into the film with positive gate voltage. Pink curve shows the current flowing into the film.

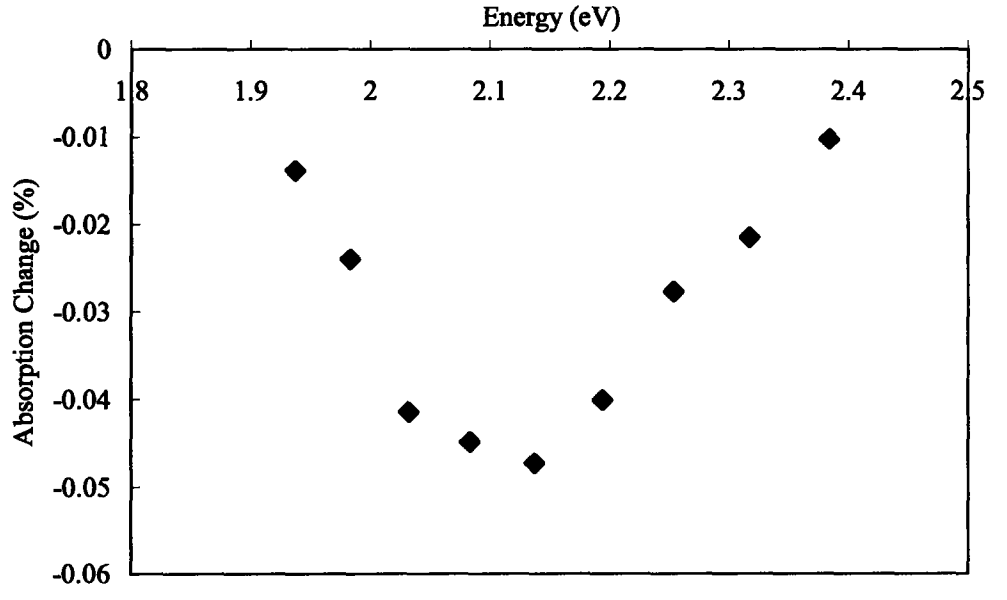

Figure 3-4: Interband transition spectrum with applied voltage of ±50 V. We observe steps for energies between 1.9 eV and 2.4 eV. The effect is strongest at approximately 2.1 eV which is close to the fluorescence peak of the nanocryatals at 2.2 eV.

3.2.2 Infrared Transitions

Figure 3-5 demonstrates the relationship between the reflected optical signal and an alternating applied gate voltage of ± 125 V at the energy of 0.22 eV. The graph is very similar to what we see in the visible region (Figure 3-3). If the steps imply the existence of the intraband transitions, the absorption should increase with injected electrons into the $1S_e$ state. On the contrary, we actually observe a decrease of absorption by injecting electrons with positive gate bias. This contradiction will be discussed in detail in the next chapter.

The FTIR spectroscopy is used to measure the spectrum of the absorption change resulting from the transitions. Figure 3-6 shows the absorption difference between +50 V and –50 V on the gate focusing on the mid-IR region, with the combination of the infrared light source, CaF_2 splitter and MCT detector. Again, the absorption spectrum shows that the nanocrystal film absorbs less when electrons are injected.

Figure 3-7 is the absorption change using a different setting for higher energies with the combination of visible light source, CaF_2 splitter and InSb detector. A valley in absorption change of about the same size is observed at the same energy as for Figure 3-6. The absorption difference is opposite to what is predicted again. Also, it is obvious there is no noticeable feature in the near-infrared range (0.5-1.2 eV).

Figure 3-8 shows the voltage dependence of the absorption change, and the magnitude of the valley (0.28 eV) at each applied voltage is plotted in Figure 3-9 with a linear fit. From the graphs, it is quite clear that the magnitude of the transition is linear in the applied electric field in the voltage range we have used.

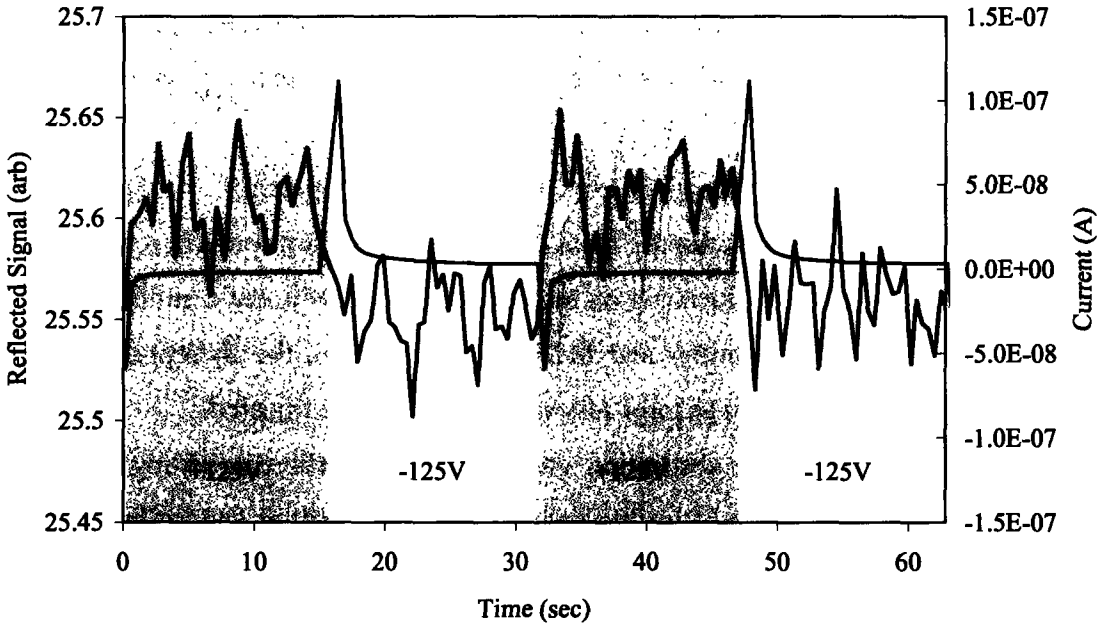

Figure 3-5: Absorption changes and current transients at 0.22 eV with applied voltageof ± 125 V. If the steps imply the existence of the intraband transitions, the absorption should increase with injected electrons into the $1S_e$ state. On the contrary, we actually observe a decrease of absorption by injecting electrons with positive gate bias.

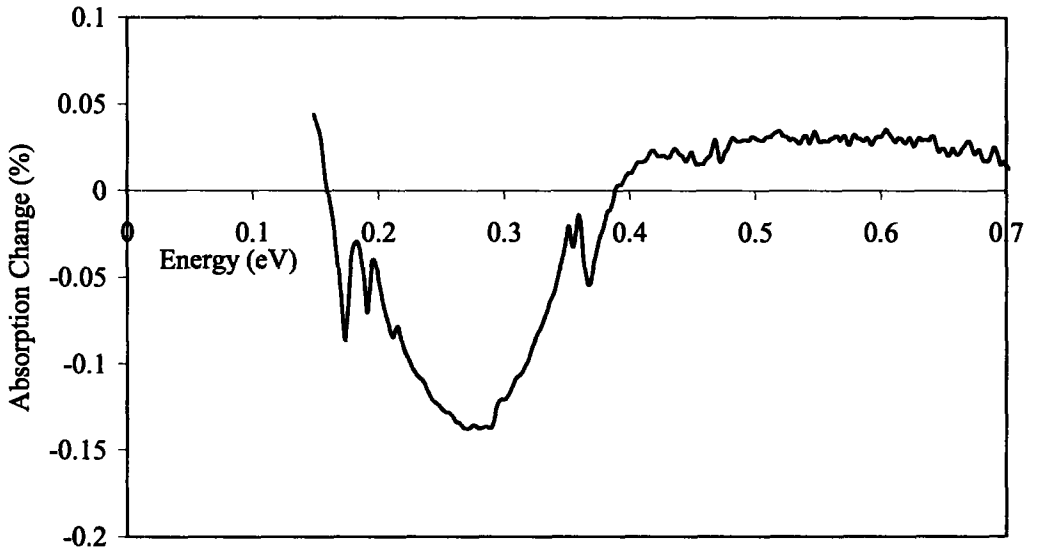

Figure 3-6: Intraband transition spectrum with applied voltage of ± 50 V focusing on the mid-IR region, with the combination of the infrared light source, CaF_2 splitter and MCT detector. It shows that the nanocrystal film absorbs less when electrons are injected as opposed to what is predicted.

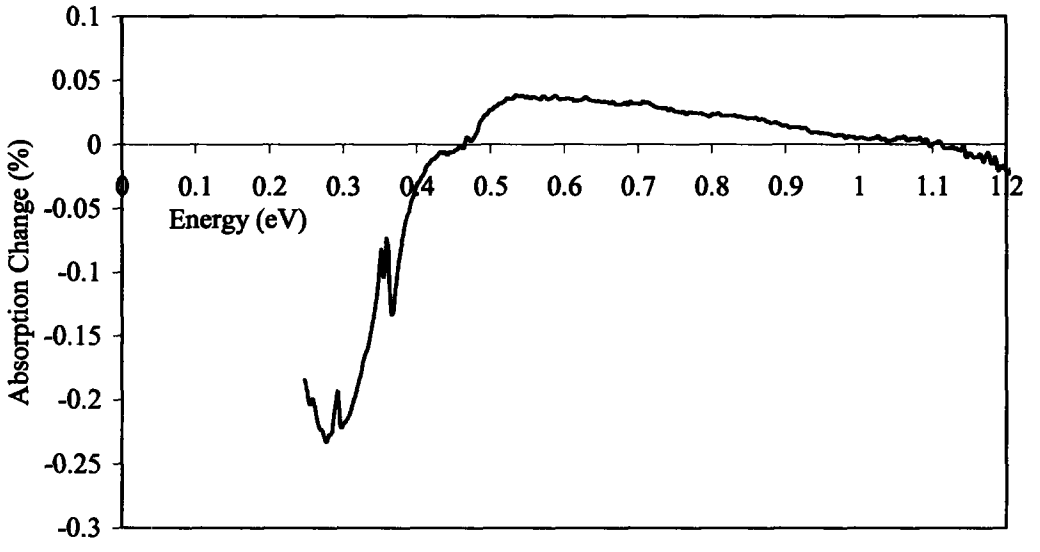

Figure 3-7: Intraband transition spectrum with applied voltage of ± 50 V focusing on the near-IR region, with the combination of visible light source, CaF_2 splitter and InSb detector. There is no noticeable feature in the near-infrared range (0.5-1.2 eV).

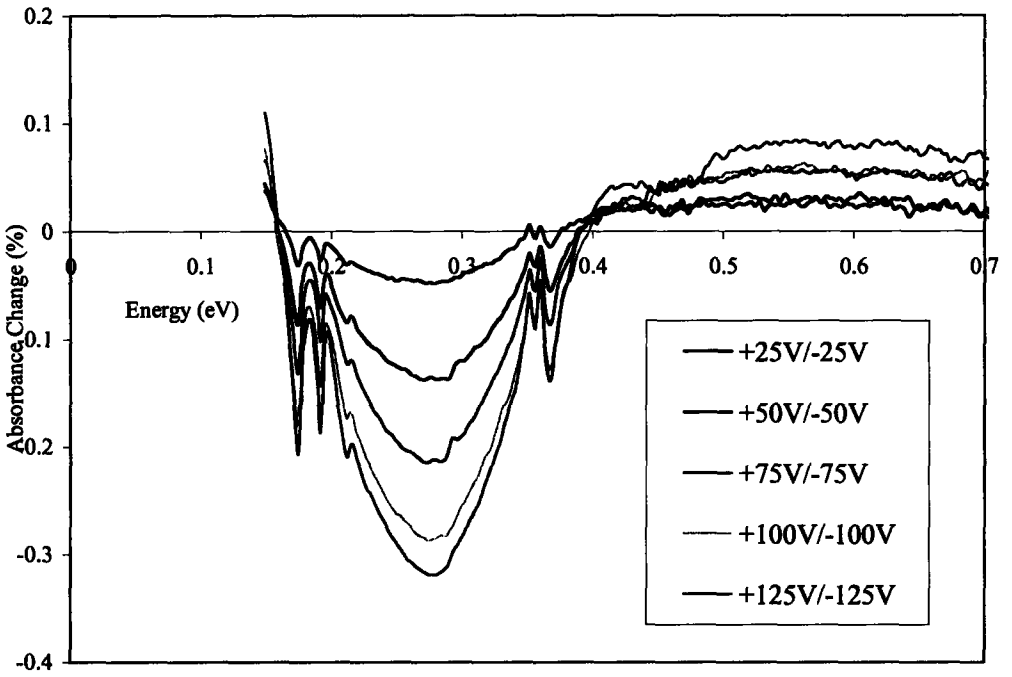

Figure 3-8: Intraband transition spectra with didffernt applied voltages.

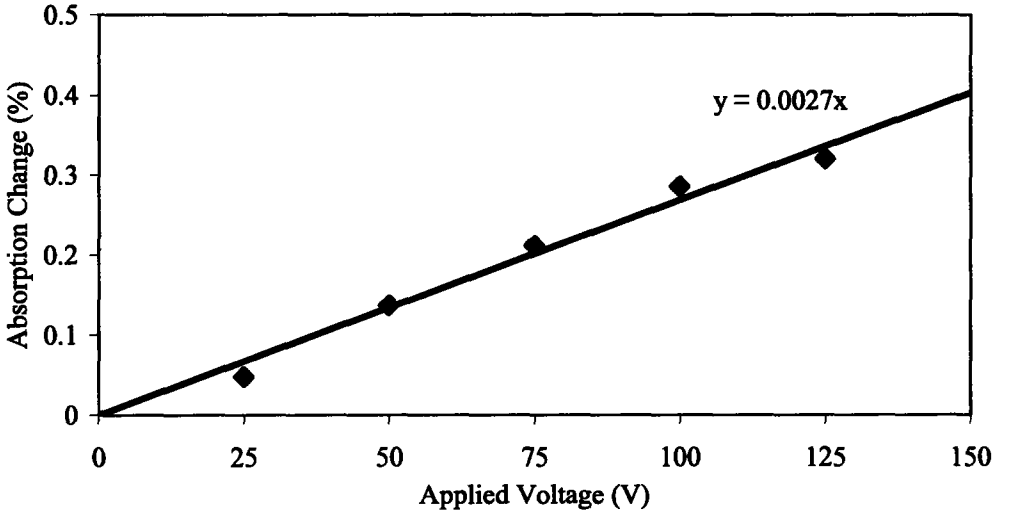

Figure 3-9: Magnitudes of intraband transition with different applied voltages. The magnitude of the transition is linear in the applied electric field in the voltage range we have used.

Chapter 4

Discussion and Analysis

4.1 General Behaviors

4.1.1 Effects of Doping

For as-grown films, we have only seen a rapid transient response to changes in gate voltage associated with the Stark effect. Only after n-type doping do we observe static changes. This suggests that the changes in undoped nanocrystals result from transient changes in the strength of the electric field inside the film, caused by the reconfiguration of the charge distribution.

On the other hand, we have seen that steady absorption changes do occur with the application of the voltage after reating the samples with sodium biphenyl. It is known that the CdSe nanocrystals can be reduced to n-type by treating with sodium biphenyl; electrons then occupy the quantum confined states of the conduction band ($1S_e$) [15]. Also it has been shown that treatment with bases, including sodium biphenyl, dramatically increases the photoconductivity as a result of increased quantum dot surface passivation [20]. From these studies, in combination with our own results, we know that the treatment enhances the conductivity of the nanocrystals by adding extra electrons in the conduction band. The surface passivation may also eliminate traps keeping the injected electrons inside the quantum dots.

4.1.2 Transition Energies

We have seen two noticeable absorption changes, one each in the visible and mid-IR regions. The observed transition energies are similar to the expected values. The valley of infrared absorption change is at 0.28 eV (seen in Figure 3-5) in fair agreement with the intraband transition energy of 0.30 eV found in photoexcited nanocrystals [14]. The absorption energy is also similar to the theoritical value of 0.35 eV obtained by effective mass calculations [21]. For the visible absorption, the valley in Figure 3-4 is found at 2.1 eV which is close to the fluorescence peak of the nanocryatals at 2.2 eV.

On the other hand, there is a clear contradiction in the directions of the response. The infrared absorption due to the intraband transitions should increase when electrons are injected with positive gate bias, but we have seen a decrease instead. Furthermore, the intraband absorption increases rather than decrease as a result of the injection of electron into the nanocrystals. The interband absorption and intraband absorption should always show opposite responses regardless of doping level, but we have seen the same sign of responses for both.

One possible explanation is that the application of the voltage simply adds disorder to the system, decreasing all absorption. Still, the energies of the two valleys in absorption change are close to the predicted interband and intraband transition energies respectively, and it is hard to say they have no relation to the interband and intraband transitions. Therefore, we still believe the results are related to interband and intraband transitions but it might be possible that more complicated mechanisms, such as hole traps, are involved into the processes. Further experiments are required to fully understand the unpredicted behavior.

4.1.3 Response Speed

Previous studies by Electric-force microscopy (EFM) have showed that the injected electrons diffuse very slowly (in the order of 10^{-3} $\mu m^2/s$) [22]. We have seen, however, the optical response changes right after the applied voltage changes as in Figure 3-3 and

3-5. Though these results seem to contradict each other, we should notice that the EFM experiment was conducted without any treatment and the results may indicate that the diffusion rate increases dramatically with treatment. In fact, treatment with cross-linking molecules has showed greatly improved electrochemical stability and speed [23] and similar by treating with sodium biphenyl.

The slow diffusion obtained in the EFM experiment might simply be the result of the injection of electrons not into the quantum dots but into the surface traps, and the diffusion rate could be improved tremendously if the treatment enhances the conductivity of the nanocrystals as predicted.

4.2 Quantitative Analysis

In this section, we estimate the change of absorption expected when electrons are injected into the nanocrystal film. Although we have shown in the previous section that interpretation of the infrared absorption change we have observed is difficult, we assume it is the result of intraband excitations and calculate the expected strength.

4.2.1 Simple Models

We estimate the magnitude of the intraband absorption here. We assume the device is a parallel plate capacitor, in which the insulating gate oxide layer is the insulator. Then, the amount of the injected charge is

$$Q = -\frac{\varepsilon A}{d} V$$

where:

d is the thickness of the gate oxide

ε is the electrical permittivity of the gate (SiO_2)

A is the surface area of the device

The minus sign means electrons (negative charges) are injected when positive charge is applied to the back gate. Therefore the number of electrons per unit area (N_e) is

$$\begin{aligned}\frac{N_e}{A} &= \frac{Q/(-e)}{A} \\ &= \frac{\varepsilon}{ed}V \\ &= \frac{(3.9)(8.85\times10^{-12}\,\mathrm{F\cdot m^{-1}})}{(1.60\times10^{-19}\,\mathrm{C/e})(3.50\times10^{-7}\,\mathrm{m})}V \\ &= 6.2\times10^{14}V\ \mathrm{m^{-2}} \\ &= 6.2\times10^{10}V\ \mathrm{cm^{-2}}\end{aligned}$$

Thus,

$$\frac{N_e}{A} = 7.8\times10^{12}\ \mathrm{cm^{-2}}\ \text{at}\ 125\,\mathrm{V}$$

In the second method, we use the electrical current we record simultaneously during the measurements and assume all the charges in the film are staying inside the quantum dots. From a previous study, we know that a power-law decay with little steady current is observed in response to a step in the applied voltage [16]. During the optical measurements, current is also measured simultaneously. By fitting the data to a power decay function, we obtain $I(t) = 5.3\times10^{-9}t^{-0.55}\,\mathrm{A}$ at 125 V. By integrating the current, the amount of the injected charge is calculated to be $Q = 1.2\times10^{-8}\,\mathrm{C}$ after one second. Therefore the number of electrons per unit area is

$$\frac{N_e}{A} = \frac{Q}{eA} = 2.1\times10^{11}\mathrm{cm^{-2}}$$

where the surface area $A = (0.60\,\mathrm{cm})^2 = 0.36\,\mathrm{cm^2}$.

4.2.2 Comparison to the Experimental Result

In this part we calculate the surface density of the charges injected into the quantum dots from the intraband absorption strength and compare to the values obtained above. To avoid long mathematical expressions, we leave some of them for the Appendix

The absorption change is

$$\frac{\Delta I}{I_0} = 1 - \exp(-\sigma c \rho \Delta t) = 1 - \exp\left(-2\sqrt{2}\sigma \frac{N_e}{A}\right) \quad \text{(in Appendix)}$$

With the parameters we used in the experiments, $2\sqrt{2}\sigma \frac{N_e}{A} << 1$. Because $\exp(x) \approx 1 + x$ for $x << 1$,

$$\frac{\Delta I}{I_0} \approx 1 - \left(1 - 2\sqrt{2}\sigma \frac{N_e}{A}\right) = 2\sqrt{2}\sigma \frac{N_e}{A}$$

This approximation agrees with the linear dependence of the absorption percentage to the applied voltage which is shown Figure 3-8 and 3-9.

Therefore, the density of the injected electrons is

$$\frac{N_e}{A} = \frac{\sqrt{2}}{4\sigma}\left(\frac{\Delta I}{I_0}\right)$$

With $\sigma = 3.9 \times 10^{-16} \frac{\omega_0}{\Delta\omega} \text{cm}^2$ calculated in Appendix, the number of electrons per unit area is

$$\frac{N_e}{A} = \frac{\sqrt{2}}{4\left(3.9 \times 10^{-16} \frac{\omega_0}{\Delta\omega} \text{cm}^2\right)}\left(\frac{\Delta I}{I_0}\right) = 9.1 \times 10^{14} \frac{\Delta\omega}{\omega_0} \frac{\Delta I}{I_0} \text{cm}^{-2}$$

In the intraband transitions, $\frac{\Delta\omega}{\omega_0} \approx 0.50$ at 125 V. The measured absorption change is $\frac{\Delta I}{I_0} \approx 3.4\times10^{-3}$ but because the effective area of the sample is only half of the total surface area (other half is covered by the electrodes), we should use $\frac{\Delta I}{I_0} \approx 6.8\times10^{-3}$ as the actual absorption change.

$$\frac{N_e}{A} = (9.1\times10^{14})(0.50)(6.8\times10^{-3})\text{cm}^{-2} = 3.1\times10^{12}\ \text{cm}^{-2}$$

This number is less than half of $7.8\times10^{12} V\ \text{cm}^{-2}$, the value obtained from the perfect capacitor model, and it may suggest not all the electrons in the films reside inside the quantum dots even after the treatment. Still, they are in the same order, which suggests the model is fairly successful as a first step.

The value obtained from the second model is about ten times smaller than the value obtained from the absorption change and it is hard to say that the model is successful. One possible explanation to this discrepancy is that huge current, beyond the power-law model, flows into the film in a moment right after the voltage is applied, which could also explain that the absorption changes occur in relatively short time (<1 second).

Chapter 5

Conclusions

We have presented results for optical measurements on charged CdSe nanocrystals. One main motivation of the project is to confirm that the injected electrons reside in quantum confined states of the dots, as opposed to traps in the organic cap layer or surface states on the dots. It can be done by monitoring changes in the visible and infrared absorption spectra. We used a diffraction grating monochromator as well as a FTIR spectrometer to obtain the absorption spectra. The measurements consist of applying voltage steps at the gate and measuring the resultant change of absorbance on the nanocrystals film.

It is expected that, with injected electrons in the $1S_e$ state of the nanocrystals, we should be able to observe the emergence of $1S_e$-$1S_p$ intraband absorption and bleaching of the interband transition. The former was observed successfully in the doped nanocrystals obtained by treating the sample with sodium biphenyl which is believed to enhance the conductivity of the nanocrystals by adding extra electrons in the conduction band. On the other hand, we also observed bleaching of the IR intraband transition instead of the predicted increase of the absorption. Though it is possible that the application of the voltage simply adds disorder to the system and it decreases all absorption, the energy and cross section of the transition are consistent with a one-electron transition between the $1S_e$ and $1P_e$ states of the strongly confined quantum dots. Therefore, we still believe the results are related to interband and intraband transitions but further experiments are required to fully understand the unpredicted behavior. I also have to mention that the step changes are not always observed even after doping. The lack of reproducibility may come from the variation of the samples.

Appendix

A.1 Absorption Change

We calculated the change in IR absorption caused by injecting electrons. In this simple calculation, we approximate that the IR beam is perfectly reflected on the SiO_2 surface. The absorption rate is

$$\frac{dI}{dt} = -\sigma c \rho I$$

where:

I is the intensity of the beam

σ is the absorption cross section of the film

c is the speed of light

ρ is the density of charged quantum dot in the film, i.e. density of injected electrons

This equation can also be integrated by the method of separation of variables

$$\int_{I_0}^{I(\Delta t)} \frac{dI}{I} = \int_0^{\Delta t} -\sigma c \rho dt$$

which yields

$$\frac{I(\Delta t)}{I_0} = \exp(-\sigma c \rho \Delta t)$$

where Δt is the time the beam takes to travel inside the film. Suppose the light is 45° to the normal of the film

$$c\Delta t = \frac{2d}{\sin 45°} = 2\sqrt{2}\,d$$

Because $\rho Ad = N_e$, the absorption change is

$$\begin{aligned}\frac{\Delta I}{I_0} &= \frac{I_0 - I(\Delta t)}{I_0} \\ &= 1 - \exp(-\sigma c \rho \Delta t) \\ &= 1 - \exp\left(-2\sqrt{2}\sigma\rho d\right) \\ &= 1 - \exp\left(-2\sqrt{2}\sigma\frac{N_e}{A}\right)\end{aligned}$$

A.2 Absorption Cross Section

Suppose the absorption spectrum of the nanocrystals forms a perfect Lorenzian function, the absorption cross section at frequency ω is [24]

$$\sigma = \frac{16\pi^2}{3}\left(\frac{e^2}{\hbar c}\right)\left(\frac{3\varepsilon_1}{2\varepsilon_1 + \varepsilon_2}\right)^2 \left|\langle 1S_e|z|1P_e\rangle\right|^2 \omega \left(\frac{1}{\pi}\frac{\Delta\omega/2}{(\omega-\omega_0)^2 + (\Delta\omega/2)^2}\right)$$

where:

ε_1 is the dielectric constant of the TOPO

ε_2 is the dielectric constant of the quantum dots (CdSe)

The maximum cross section at ω_0 is

$$\begin{aligned}\sigma &= \frac{16\pi^2}{3}\left(\frac{e^2}{\hbar c}\right)\left(\frac{3\varepsilon_1}{2\varepsilon_1 + \varepsilon_2}\right)^2 \left|\langle S_e|z|P_e\rangle\right|^2 \omega_0 \left(\frac{2}{\pi\Delta\omega}\right) \\ &= \frac{32\pi}{3}\left(\frac{e^2}{\hbar c}\right)\left(\frac{3\varepsilon_1}{2\varepsilon_1 + \varepsilon_2}\right)^2 \left|\langle S_e|z|P_e\rangle\right|^2 \frac{\omega_0}{\Delta\omega}\end{aligned}$$

Using the Bassel function solutions for the spherical box with infinite barrier potential, one has $\langle S_e|z|P_e\rangle \approx 0.306 r_0$ where r_0 is the radius of the quantum dot.

Let:

$$\frac{e^2}{\hbar c} = \frac{1}{137}$$

$\varepsilon_1 = 2$ (TOPO)

$\varepsilon_2 = 6.3$ (CdSe)

$$\langle 1S_e|z|1P_e\rangle \approx 0.306 r_0 = (0.306)\left(\frac{4.5\times10^{-7}\,\text{cm}}{2}\right) = 6.9\times10^{-8}\,\text{cm}$$

Then,

$$\sigma = \frac{32\pi}{3}\left(\frac{1}{137}\right)\left(\frac{3(2)}{2(2)+(6.3)}\right)^2 (6.9\times10^{-8}\,\text{cm})^2\left(\frac{\omega_0}{\Delta\omega}\right)$$

$$= 3.9\times10^{-16}\,\frac{\omega_0}{\Delta\omega}\,\text{cm}^2$$

Bibliography

[1] L.W. Ji, Y.K. Su, S.J. Chang, S.H. Liu, C.K. Wang, S.T. Tsa, T.H. Fang, L.W. Wu, and Q.K. Xue. InGaN quantum dot photodetectors. *Solid-State Electronics*, 47:1753-1756, 2003.

[2] Seth Coe, Wing-Keung Woo, Moungi Bawendi, and Vladimir Bulovic. Electroluminescence from single monolayers of nanocrystals in molecular organic devices. *Nature*, 420:800-803, 2002.

[3] Xiaoqin Li, Yanwen Wu, Duncan Steel, D. Gammon, T.H. Stievater, D. S. Katzer, D. Park, C. Piermarocchi, and L.J. Sham. An All-Optical Quantum Gate in a Semiconductor Quantum Dot. *Science*, 301:809-811, 2003.

[4] Eliana Biolatti, Rita C. Iotti, Paolo Zanardi, and Fausto Rossi. Quantum Information Processing with Semiconductor Macroatoms. *Physical Review Letter*, 85:5647-5650, 2000

[5] Islamshah Amlani, Alexei O. Orlov, Geza Toth, Gary H. Bernstein, Craig S. Lent, and Gregory L. Snider, Digital Logic Gate Using Quantum-Dot Cellular Automata. *Science*, 284:289-291, 1999.

[6] M. Girlanda, M. Governale, M. Macucci, and G. Iannaccone. Operation of quantum cellular automaton cells with more than two electrons. *Applied Physics Letter* 75:3198-3200, 1999.

[7] Paul Alivisatos. The use of nanocrystals in biological detection. *Nature Biotechnology*, 22:47-52, 2004.

[8] Benoit Dubertret, Paris Skourides, David J. Norris, Vincent Noireaux, Ali H. Brivanlou, and Albert Libchaber. In Vivo Imaging of Quantum Dots Encapsulated in Phospholipid Micelles. *Science*, 298:1759-1762, 2002.

[9] M.A. Kastner. Artificial atoms. *Physics Today*, 46:24-31, 1993.

[10] R.C. Ashoori. Electrons in artificial atoms. *Nature*, 379:413-419, 1996

[11] Konstantin K. Likharev. Single Electron Devices and Their Applications. *Proceedings of the IEEE*, 87:606-632, 1999.

[12] C.B. Murray, C.R. Kagan CR, and M.G. Bawendi. Synthesis and characterization of monodisperse nanocrystals and close-packed nanocrystal assemblies. *Annual Review of Materials Science*, 30:545-610, 2000.

[13] C.P. Collier, T. Vossmeyer, and J. R. Heath. Nanocrystal Superlattices. *Annual Review of Physical Chemistry*, 49:371-404, 1998.

[14] Moonsub Shim, Sergej V. Shilov, Mark S. Braiman, and Philippe Guyot-Sionnest. Long-lived delocalized electron states in quantum dots: a step-scan Fourier transform infrared study. *Journal of Physical Chemistry B*, 104:1494-1496, 2000.

[15] Moonsub Shim and Philippe Guyot-Sionnest. n-type colloidal semiconductor nanocrystals. *Nature*, 407:981-983, 2000.

[16] Nicole Y. Morgan, C.A. Leatherdale, M. Drindic, Mirna V. Jarosz, Marc A. Kastner, and Moungi Bawendi. Electronic transport in films of colloidal CdSe nanocrystals. *Physical Review B*, 66:075339, 2002.

[17] M.V. Jarosz, N.E. Stott, M. Drndic, N.Y. Morgan, M.A. Kastner, and M.G. Bawendi. Observation of bimolecular carrier recombination dynamics in close-packed films of colloidal CdSe nanocrystals. *Journal of Physical Chemistry B*, 107:12585-12588, 2003.

[18] James W. Cooley and John W. Tukey. An Algorithm for the Machine Calculation of Complex Fourier Series. *Mathematics of Computation*, 19:297-301, 1965

[19] A. Sacra, D. J. Norris, C. B. Murray, and M.G. Bawendi. Stark spectroscopy of CdSe nanocrystallites: The significance of transition linewidths. *Journal of Chemical Physics*, 103:5236-5245, 1995.

[20] M.V. Jaroz, V.J. Porter, B.R. Fisher, M.A. Kastner, and M.G. Bawendi. Photoconductivity Studies of Treated CdSe Quantum Dot Films Exhibiting Increased Exciton Ionization Efficiency. To be published, 2004.

[21] D.J. Norris and M.G. Bawendi. Measurement and assignment of the size-dependent optical spectrum in CdSe quantum dots. *Physical Review B*, 53:16338-16346, 1996.

[22] M. Drndic, R. Markov, M.V. Jarosz, M. G. Bawendi, M.A. Kastner, N. Markovic, and M. Tinkham. Imaging the charge transport in arrays of CdSe nanocrystals. *Applied Physics Letters*, 83:4008-4010, 2003.

[23] Philippe Guyot-Sionnest and Congjun Wang. Fast Voltammetric and Electrochromic Response of Semiconductor Nanocrystal Thin Films. *Journal of Physical Chemistry B*, 174:7355-7359, 2003.

[24] P. Guyot-Sionnest and M.A. Hines. Intraband transitions in semiconductor nanocrystals. *Applied Physics Letters*, 72:686-688, 1998.